Astronomical Techniques and Instruments, Vol. 2, November 2025, 339–347

Article **Open Access**

Design and analysis of a direct-drive motor for astronomical telescopes in extreme Antarctic environments

Yao Zhang[1,2,3], Qingshan Li[4], Zhengyang Li[1,2*], Xiaoyan Li[1,2], Zhenshuai Yan[1,2,3], Jia'nan Cong[1,2,3]

[1]*Nanjing Institute of Astronomical Optics & Technology*, *Chinese Academy of Sciences*, *Nanjing* 210042, *China*
[2]*CAS Key Laboratory of Astronomical Optics & Technology*, *Nanjing Institute of Astronomical Optics & Technology*, *Nanjing* 210042, *China*
[3]*University of Chinese Academy of Sciences*, *Beijing* 100049, *China*
[4]*Astro Engineering Co.*, *Ltd.*, *Tianjin* 300382, *China*

*Correspondence: zyli@niaot.ac.cn

Received: June 28, 2025; Accepted: August 25, 2025; Published Online: August 26, 2025; https://doi.org/10.3724/ati2025053; https://cstr.cn/32083.14.ati2025053

Citation: Zhang, Y., Li, Q. S., Li, Z. Y., et al. 2025. Design and analysis of a direct-drive motor for astronomical telescopes in extreme Antarctic environments. *Astronomical Techniques and Instruments*, **2**(6): 339−347. https://doi.org/10.3724/ati2025053.

Abstract: Effective motors are crucial for driving astronomical telescopes, especially for those operating in Antarctica, where the harsh environment and operating conditions, including extreme low temperature, ice/snow accumulation, low power consumption, and unattended operation, introduce challenges to the design and development of motor drives. We present the design of a permanent magnet synchronous motor suitable for this environment, conducting a quantitative analysis on the impacts of cryogenic conditions on lubricant performance, differential thermal contraction of metallic components, and remanent flux density of neodymium iron boron (N52) permanent magnets. We also implement a labyrinth seal structure, combined with silicone sealing rings, to mitigate ice crystal intrusion risks. Finite element analysis and laboratory tests demonstrate a maximum torque output of 25 Nm. This kind of motor is used in the Antarctic 15 cm Near Infrared Telescope at Dome A, Antarctica. Operation data shows a total encoder feedback error of 0.0678" for the telescope control system with 15" s^{-1} tracking speed at −56.79°C. These results comprehensively validate the high reliability and precision of the motor under the extreme conditions of the polar environment.

Keywords: Axial flux motor; Low temperature; 3D finite element analysis; Antarctic astronomical telescope; Dome A

1. INTRODUCTION

The Antarctic plateau offers exceptional astronomical observation conditions. Dome A, the highest point on the Antarctic plateau, presents ideal conditions for astronomical observation. It is characterized by extremely low temperatures ranging from −80°C to −30°C, a high altitude of 4093 m above sea level, low water vapor content, clear sky background, and a high frequency of clear nights with more than three months of continuous observation possible during polar night[1]. Measurements with the Kunlun Differential Image Motion Monitor (KL-DIMM) show a median free-atmosphere seeing of 0.31", and located at a height of just 8 m, the recorded seeing is as low as 0.13", surpassing the capabilities of other renowned terrestrial observation sites[2]. Capitalizing on these conditions, telescopes have been deployed by Chinese research teams at Dome A since 2008[3].

Dome A exhibits severe climatic extremes with pronounced seasonal variability. Meteorological records show an annual temperature range spanning over 55°C, with median daily temperatures approaching −35°C during January to February and plunging below −80°C throughout June to August[4]. Critically, diurnal temperature variations frequently surpass 10°C, generating substantial thermal stress on instrumentation. These conditions create specific operational challenges for telescope drive systems, including degradation of material properties and electromagnetic performance at cryogenic temperatures, persistent risks of invasion of snow/ice, energy constraints at the Antarctic site, and the logistical constraint of unattended operation at Kunlun Station, located at Dome A, where annual maintenance windows are limited to approximately 20 days. These conditions necessitate electromechanical reliability, extended service longevity, and highly efficient energy usage.

Precision astronomical mounts demand servo systems capable of stable pointing, sidereal tracking, and dynamic target acquisition under extreme conditions. Traditional gear-driven systems have inherent limitations, including structural complexity, elevated failure probability, maintenance intensity, excessive noise and vibration, and low transmission efficiency[5]. To overcome these limitations, we present an axial-flux permanent magnet (PM) synchronous motor (AF-PMSM) with a direct-drive system. This integrated approach eliminates transmission components, reducing the possibility of the system becoming stuck owing to snow and ice. The AF-PMSM gives essential advantages, including high torque density and compact form factor through its axial magnetic flux configuration. Concurrently, a direct-drive implementation offers fundamental performance benefits through elimination of backlash and wear mechanisms inherent in geared systems, yielding improved transient response, reduction of acoustic noise, and simplification of maintenance protocols because of the reduced component count[6].

Here, we present a type of AF-PMSM which is used in the Antarctic 15 cm Near Infrared (NIR) Telescope at Dome A. With a 150 mm aperture, this telescope adopts a modified hyperbolic Newtonian design with a wavelength range of 1.1–1.4 μm. The detector has dimensions of 6.4 × 5.12 mm and a pixel ratio of 2.46". The telescope mount has a mass of 63 kg and a rotation radius of 310 mm, while the telescope tube assembly has a mass of 5.23 kg and a rotation radius of 300 mm. Consequently, we design a coreless AF-PMSM with a 340 mm outer diameter.

In this paper, we present a finite element analysis (FEA) in Section 2 and discuss the challenges encountered by motors in Antarctic conditions and the corresponding engineering solutions in Section 3. We report the laboratory test results of the mount and the operational performance of the telescope in Antarctica in Section 4, and then draw our conclusions.

2. FEA OF MOTOR PERFORMANCE

2.1. Basic Parameters of the Motor

The motor design considers telescope structural parameters, transportation constraints, and Antarctic operational conditions to meet the core requirements of high-precision positioning and rapid response. The motor is configured with an 18-coil/24-pole, single-stator-single-rotor topology and surface-mounted N52 magnets (8 × 23 × 38 mm) as shown in Fig. 1. Electromagnetically, the 24 poles effectively suppress cogging torque and torque ripple, ensuring operational smoothness. Mechanically, the stator outer diameter of 340 mm provides the required maximum torque of 25 Nm for driving the load, while the 200 mm inner diameter offers ample space for internal components. Magnetically, the 1.3 mm air gap thickness, combined with the 8 mm magnet thickness, optimizes efficiency while maintaining adequate flux density. The integrated driver supports a maximum current of 8 A, enabling a maximum operational speed of 12° s^{-1} within a power rating of 240 W. Key design specifications are detailed in Table 1.

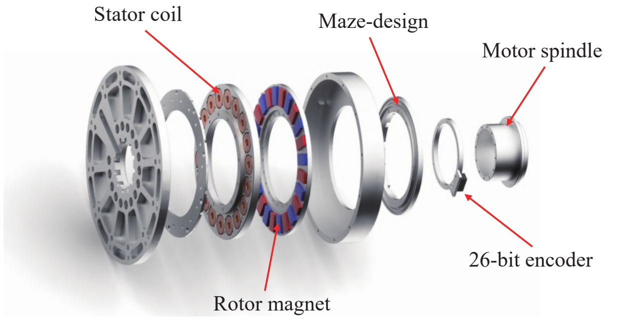

Fig. 1. The structure of the direct-drive motor.

Table 1. Motor specifications

Parameter	Value
Stator coils	18
Number of poles	24
Air-gap thickness/mm	1.3
Outer diameter of stator/mm	340
Rotor PM thickness/mm	8
Rated power/W	240
Rated voltage/V	48
Inner diameter of stator/mm	200

Compared with radial-flux motors, AF-PMSMs offer superior diameter-to-length ratios and flatter air gaps[7], enabling lower noise/vibration, higher efficiency, and enhanced air gap tolerance. The coreless topology eliminates ferromagnetic materials, suppressing most eddy current and core losses[8] through torque generation via conductor-PM field interaction.

2.2. 3D FEA of Motor Electromagnetic Characteristics

For electromagnetic simulation, we use the Maxwell software to model the motor and analyze its performance parameters under various operating conditions. During the simulation calculations, we neglect leakage flux and edge effects.

Based on fundamental motor operating principles, we derive the electromagnetic relationships using the equivalent magnetic circuit method[9], expressed as

$$E_{\mathrm{f}} = \frac{\sqrt{2}\pi^2}{8} n_\delta N k_{\mathrm{w}} \alpha_i B_\delta (D_{\mathrm{out}}^2 - D_{\mathrm{in}}^2), \tag{1}$$

$$P_{\mathrm{e}} = \frac{\pi^3}{32} n_{\mathrm{s}} k_{\mathrm{w}} A_{\mathrm{av}} \alpha_i B_\delta (D_{\mathrm{out}} + D_{\mathrm{in}})(D_{\mathrm{out}}^2 - D_{\mathrm{in}}^2), \tag{2}$$

and

$$T_{\mathrm{e}} = \frac{P_{\mathrm{e}}}{2\pi n_{\mathrm{s}}} = \frac{\pi^2}{64} k_{\mathrm{w}} \alpha_i B_\delta (D_{\mathrm{out}} + D_{\mathrm{in}})(D_{\mathrm{out}}^2 - D_{\mathrm{in}}^2). \tag{3}$$

In these equations, E_{f} is the induced electromotive force of the motor, P_{e} is the electromagnetic power of the motor, T_{e} is the electromagnetic torque of the motor, n_{s} is the synchronous speed of the motor, k_{w} is the winding factor, A_{av} is the average armature area of the motor, α_i is the phase angle of the current, B_δ is the air-gap flux density, D_{out}, and D_{in} are the outer and inner diameters of the motor, respectively.

The simulation analyzes motor operation at 1 A excitation with a rotational velocity of 12° s^{-1}. As shown in Fig. 2, the resultant flux density distribution remains consistently below 1.6 T.

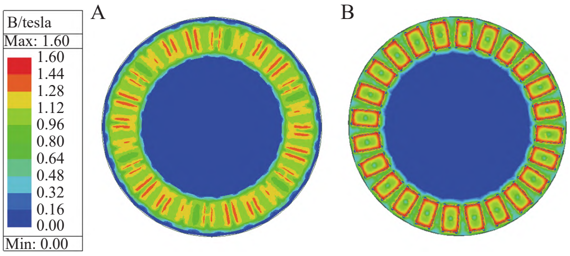

Fig. 2. Comparative simulation of magnetic flux density distribution in cored and coreless motor cross-sections. (A) Iron-core motor. (B) Coreless motor.

Based on our simulation results (shown in Fig. 3), we compare the torque of coreless motors and cored motors using the sliding window method and find that under rated working conditions (48V, 5A), the working torque of coreless motors is more stable. The average torque of the cored motor is 11.93 Nm with a maximum fluctuation of 4.067 Nm, and the average torque of the coreless motor is 11.36 Nm with a maximum fluctuation of 0.37 Nm. Under the same conditions, the torque fluctuation of coreless motors is less than that of cored motors, making them more suitable for low-speed, high-precision rotation.

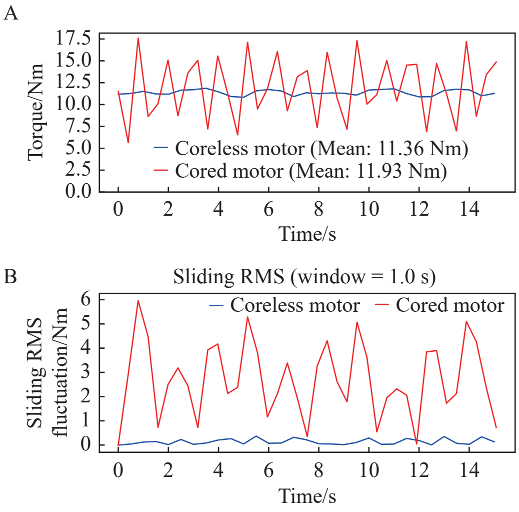

Fig. 3. Comparative analysis of torque output and fluctuation. (A) Time-domain torque output of the coreless and cored motors. (B) Sliding root-mean-square (RMS) torque fluctuation.

We perform sector-shaped scanning of the air gap between PMs and windings, at radial positions from 11.5 cm to 15.5 cm, yielding the flux density distribution (see Fig. 4). With the reference point at a 13.5 cm radius (midpoint of 0.13 cm air gap), the maximum flux density reaches 1.6 T, and the minimum measures −1.25 T.

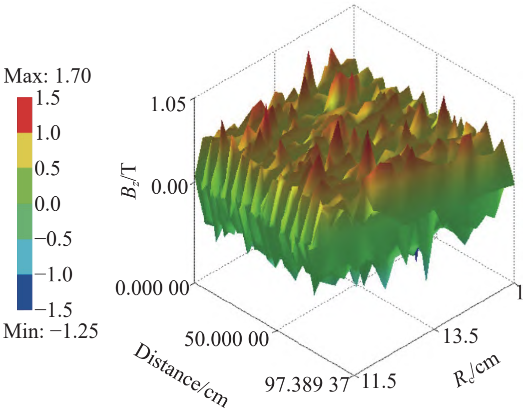

Fig. 4. Sector-scanned 3D flux density distribution in the motor air gap. The scan was performed radially from 11.5 cm to 15.5 cm. B_z is the magnetic flux density in the Z direction, and R_c is the radius of the motor.

Following the analysis of fundamental motor parameters, we perform a torque simulation at varying temperatures while maintaining constant operating parameters. As shown in Fig. 5, when the temperature decreases from room temperature to −80°C, the average torque increases from 3.24 Nm to 3.65 Nm, representing a 12% variation rate in low-temperature torque. However, the operational resistance of the motor also rises, primarily as a result of the viscosity of the bearing grease and thermal contraction-induced preload elevation at aluminum-steel interfaces.

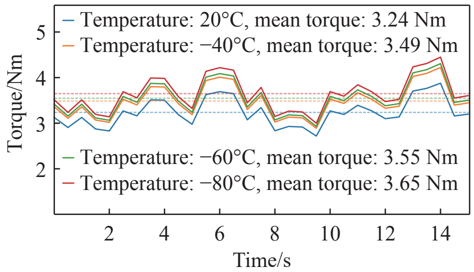

Fig. 5. Torque performance of the motor at various temperatures.

3. ANALYSIS AND DESIGN FOR THE ANTARCTIC ENVIRONMENT

3.1. Low-temperature Effect on the Bearing Grease

The motor bearing critically governs the reliability of a telescope transmission system, because bearing lubrication strongly determines its lifespan. Grease, comprising a base oil, thickener, and additives, is the primary lubricant, with the base oil constituting over 65%. Grease forms a lubricating film to minimize mechanical wear between bearing components by separating surfaces, while sealing against contaminant ingress and dissipating heat caused by friction. To perform these functions, grease must possess adequate fluidity. Diminished grease fluidity at low temperatures elevates starting torque and friction losses, necessitating careful selection of the type of grease used. The primary selection criteria require the grease to remain non-solidified at operating temperatures while retaining sufficient viscosity for lubrication.

Direct-drive telescopes operate at exceptionally low angular velocities, typically ranging from 15″ s^{-1} to 5° s^{-1}. Hence, grease failures at high-temperature, caused by high-speed rotation, are eliminated, but this situation creates critical challenges in low-temperature lubrication. The low temperature and low speed reduce molecular mobility within the grease, strengthening intermolecular interactions and significantly increasing viscosity. This viscosity surge critically impairs oil film formation capability[10].

Two viable methods exist to alleviate this problem. The first approach entails the application of commercial aerospace greases. When compared with common grease, which typically exhibits a starting torque temperature break point above −22°C[11], aerospace grease can operate effectively within a temperature range extending down to −95°C. It maintains a starting torque of 0.58 Nm and an operating torque of 0.19 Nm at −95°C. These attributes prevent grease solidification, minimizing initial rotational resistance and providing the robust adhesion and moldability essential for reliable mechanical operation.

The second method is to remove the common grease from the motor bearings. As shown by experimental studies[12], the viscosity of ordinary grease follows an exponential growth pattern as temperature decreases, which escalates the load torque. Moreover, the hysteretic behavior inherent in the viscosity variation of such grease induces non-linear load characteristics. In contrast, removing conventional grease reduces load non-linearity, significantly decreasing load torque and effectively preventing the failure of rotary motion.

3.2. Low-temperature Effects on the Properties of Non-magnetic Metal Materials

Considering the extreme conditions in Antarctica, which demand structural materials combining light weight, corrosion resistance, and brittle fracture resistance, the rotor disc, which also serves as the shell for the bearing, is constructed from 6061 aluminum alloy. When the ambient temperature changes, different metal materials exhibit varying amounts of elastic deformation. In this case, the aluminum shell exhibits greater thermal shrinkage than the steel bearing, which leads to increased friction torque within the drive system, ultimately compromising the reliability of the entire system.

When the temperature drops from 20°C to −80°C, the average pressure between the shell and the outer ring of the bearing is 36.4 MPa (see Fig. 6). The maximum simulated deformation difference between the shell and the outer diameter of the bearing at −80°C is 0.0023 mm.

3.3. Low-temperature Effects on Motor Electromagnetic Performance

The impact of temperature on PMs is primarily reflected in the changes of remanence and coercivity. The stability of PMs is represented by the temperature coefficient, given by

$$\alpha=\left[\frac{B_{\mathrm{r}}(t_1)-B_{\mathrm{r}}(t_0)}{B_{\mathrm{r}}(t_0)\times(t_1-t_0)}\right]\times 100\%, \tag{4}$$

where α is the percentage change rate per unit time, and $B_{\mathrm{r}}(t_0)$ and $B_{\mathrm{r}}(t_1)$ are the remanence at the initial time t_0 and the subsequent time t_1, respectively. The PM material used in this design is sintered neodymium iron boron, N52. At room temperature (20°C), it has a remanence of 1.43 T and a coercivity of 1138 kA m^{-1}. The temperature coefficient of remanence is −0.12% which means in a −80°C environment, the magnetic strength of N52 is 1.12 times that at 20°C. The temperature coefficient of coercivity is −0.6%. We find that N52 can be used as a PM material in Antarctic telescope motors.

3.4. The Maze-design Structure

Although atmospheric precipitation is scarce in the Dome A region, loose snow can easily be lifted by strong winds, leading to the invasion of ice and snow into machinery; ice particles can infiltrate the interior of the motor through sealing gaps, leading to an increase in the friction coefficient of the bearings. Ice tends to adhere to metal surfaces in low-temperature environments, forming an ice film which increases the viscous resistance of moving parts.

To mitigate the impact of invasion of ice on the motor, our design incorporates a maze-like structure, consisting of a series of multiple complex passages and barriers that prevent the invasion of ice. As shown in Fig. 7, each turn and path adds an extra layer of protection, making it extremely difficult for contaminants to enter. This structure will effectively prevent contaminants from entering the motor without increasing the frictional torque of the motor caused by thermal expansion and contraction.

This motor is designed with cogging at a width of 3 mm, and backlash with a width of 1 mm. The backlash is filled with a silicone seal, which can withstand low temperatures down to −73°C. Because the labyrinth seal has no complex mechanical parts in its structural design, it is generally easy to maintain and replace. The labyrinth seal is suitable for such extreme environments because it provides a physical barrier for the motor, capable of withstanding extreme temperature changes and harsh weather conditions.

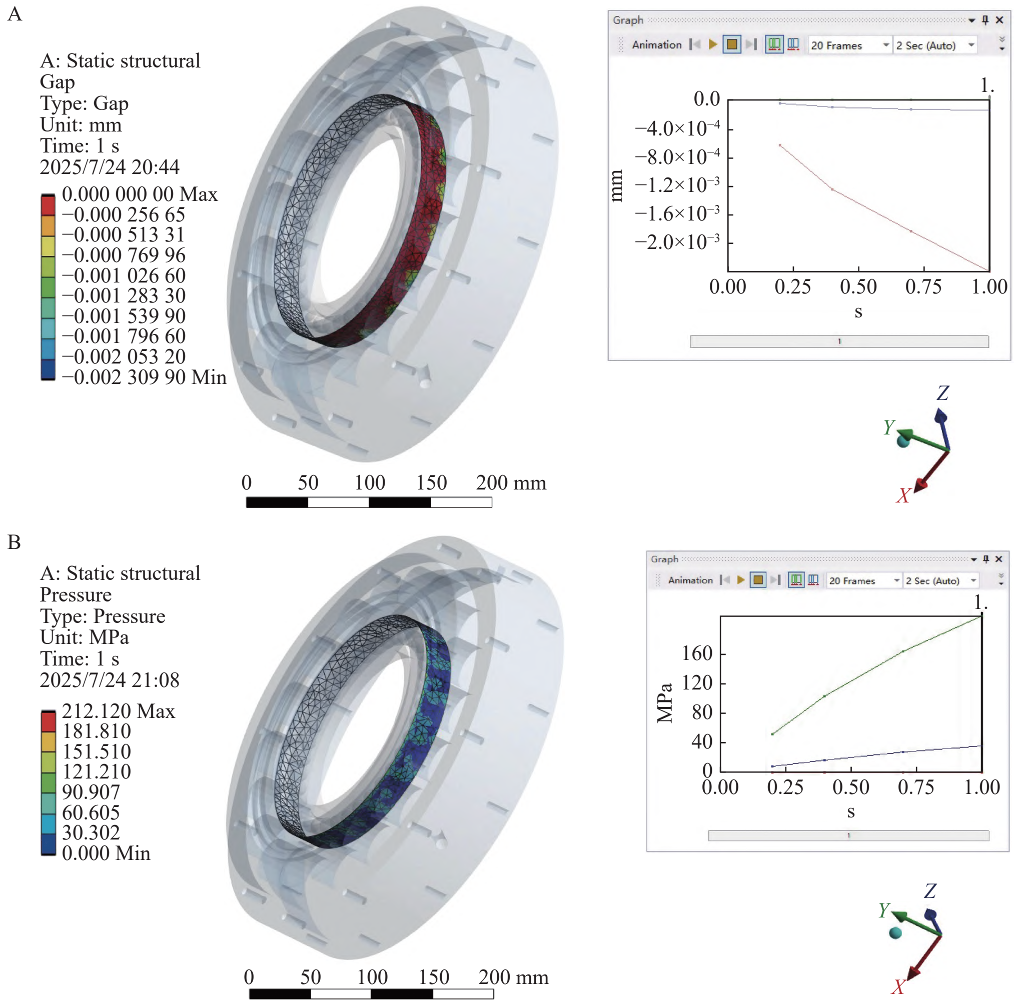

Fig. 6. Analysis of thermal-induced mechanical response. (A) Variation of the structural gap between the housing and bearing as temperature decreases from 20°C to −80°C. (B) Corresponding contact pressure distribution on the bearing outer race.

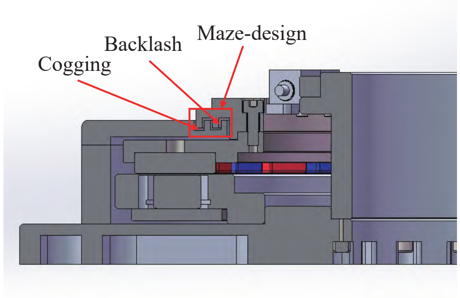

Fig. 7. Longitudinal-sectional view of the proposed AF-PMSM.

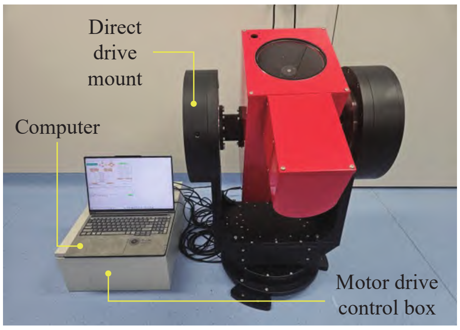

Fig. 8. Photograph showing the near-infrared telescope at the laboratory, Nanjing.

4. RESULTS

4.1. Test Results

The 150 mm aperture telescope control system consists of a control computer, a control box and the tested direct drive mount (see Fig. 8). It is subjected to magnetic induction testing, torque testing, and operating accuracy testing.

While slewing, the magnetic flux density of the telescope rotor disc measures 278.5 mT, as shown in Fig. 9. The slew speed of the motor is 12° s^{-1}, which is the maximum speed set by the control board. Fig. 10 shows the measured motor torque at different currents, along with the fitting curve. By calculating the slope of the fitting curve using the ordinary least squares method, we find the torque coefficient of the motor to be 3.76 Nm A^{-1}.

4.2. Measured Results at Different Temperatures

Antarctic 15 cm NIR Telescope was successfully installed in 2024 January at Dome A, and is shown in Fig. 11. Alongside laboratory tests, our measurement data

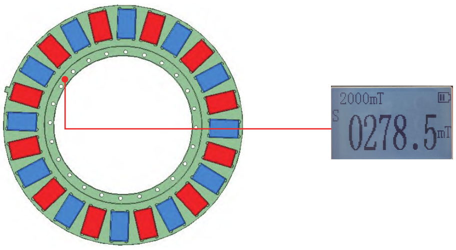

Fig. 9. Surface flux density mapping of the telescope rotor disc during a slewing operation. The measurement was performed at the maximum slew speed of the motor, of 12° s^{-1}.

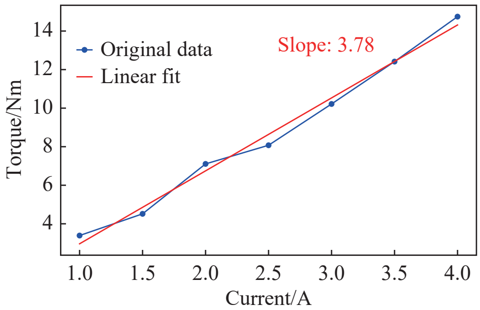

Fig. 10. Linear relationship between torque and current. Measured data (blue) and linear fit (red) for the motor during testing at 20 °C.

includes on-site telescope telemetry from Dome A, acquired using high-precision temperature sensors and digital encoders. We use a 26-bit encoder with an angular resolution of 0.018". Continuous motor encoder data streams are sampled at 9 Hz at precisely 5-min intervals (yielding 2 700 datapoints per measurement cycle), enabling time-resolved analysis of electromechanical performance under different environmental conditions.

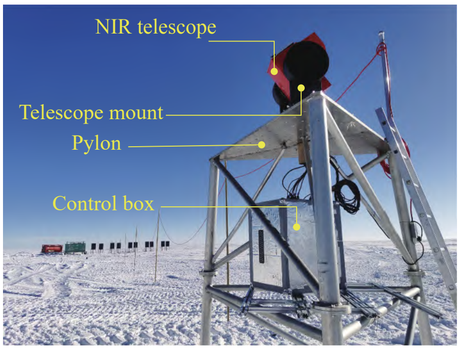

Fig. 11. Photograph showing the NIR telescope at Kunlun Station, Dome A.

The motor tracking error, as detailed in Fig. 12, is precisely measured in the laboratory at 20°C with a speed of 15" s^{-1}. On the basis of encoder readings, we calculate RMS errors for both telescope axes.

The total RMS pointing error, RMS_{Total}, is calculated as

$$RMS_{\text{Total}} = \sqrt{(\Delta Alt)^2 + (\Delta Az)^2}, \tag{5}$$

where ΔAlt is the RMS error in the altitude axis and ΔAz is the RMS error in the azimuth axis. Applying Equation (5) yields a total encoder feedback tracking error of 0.039" at 20°C.

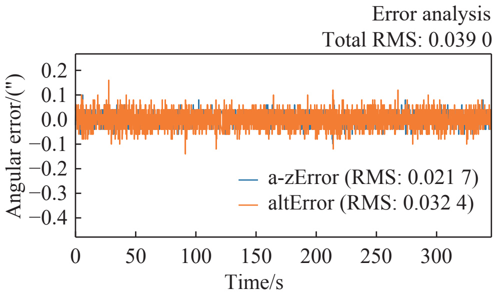

Fig. 12. Encoder error of the motor during a 5-min period at the laboratory, Nanjing.

Fig. 13 shows the temperature profile and tracking error at Kunlun Station, recorded on March 4, 2025, with the daily minimum occurring between 18:00–20:00 universal time (UT). Consequently, the telescope mount tracking error analysis focuses on the time period 18:50–18:55 (UT), where the average ambient temperature measured is −56.79°C. The measured error of the altitude axis of the telescope is 0.034 8", and the error of the azimuth axis is 0.058 2". Using Equation (5), we calculate that at −56.79°C, the overall encoder feedback tracking error of the telescope is 0.067 8". Compared with the pixel ratio of 2.46", this tracking error meets the required telescope precision.

The data from 5:10–5:15, March 5, 2025 (UT) are similarly processed (see Fig. 14). During this period, the average temperature at Kunlun Station is −48.45°C, and the overall tracking error of the telescope is 0.047 2". This further confirms that the tracking performance of the telescope remains within the required precision range under different temperature conditions.

Comparative analysis of encoder feedback tracking errors at 20°C and −56.79°C reveals a 0.028 8" variation within this 76°C temperature range. Both values satisfy the design specifications for motor performance across the operational temperature range.

We assess tracking performance during polar night by continuously observing the star HIP 41037 for 5 min using 0.1 s exposures. As shown in Fig. 15, after compensating low-order tracking errors via least-squares fitting of the pointing model (applicable during polar night), we measure the residual RMS tracking error to be 0.243" at −65°C, based on centroid coordinate fluctuations[13].

5. DISCUSSION AND CONCLUSIONS

The design and analysis of the AF-PMSM for the Antarctic 15 cm NIR Telescope demonstrate its suitability for the extreme environmental conditions at Dome A in Antarctica. The performance of the motor at low temperatures and potential invasion of ice has been carefully considered by material and structural optimization to effectively address the challenges posed by the Antarctic envi-

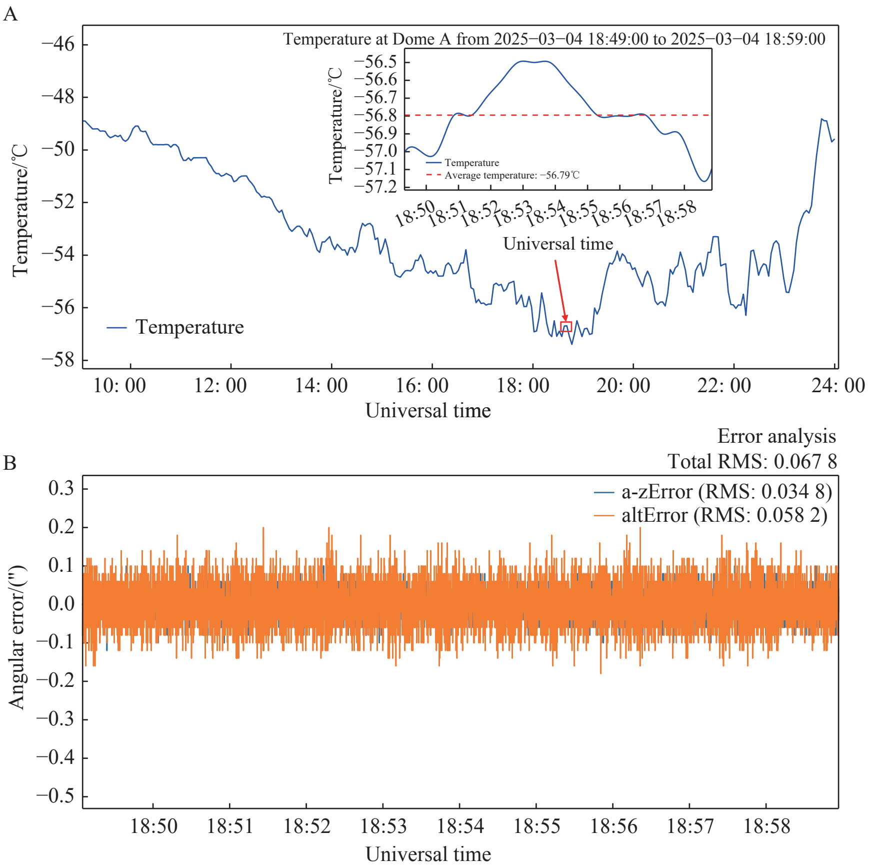

Fig. 13. Ambient temperature and motor encoder accuracy at Dome A, Antarctica, March 4, 2025. (A) Diurnal temperature record at Kunlun Station. (B) Encoder error of the motor during a 5-min period during the daytime temperature minimum.

ronment.

Our FEA results provide valuable insights into the performance of the motor, and the electromagnetic simulation and torque comparison between coreless and core motors have highlighted the advantages of the coreless design in terms of low torque ripple at low speeds and low currents. We find that it is more suitable for high-precision applications. For future iterations with increased payload mass, the dual-rotor-single-stator (DRSS) configuration may enhance torque capacity while maintaining cryogenic operational stability.

Laboratory tests, including magnetic induction testing, torque testing, and operating accuracy testing, have validated the consistency between motor performance and simulation results. The processing and analysis of on-site operating data of the Antarctic 15 cm NIR Telescope at Dome A show that the tracking precision of the telescope reaches 0.067 8" at −56.79°C.

In conclusion, our motor design offers a robust and high-precision solution for the Antarctic 15 cm NIR Telescope. The combination of FEA, laboratory testing, and on-site measurement data at Dome A provides a comprehensive assessment of motor performance. This study not only contributes to the advancement of astronomical obser-

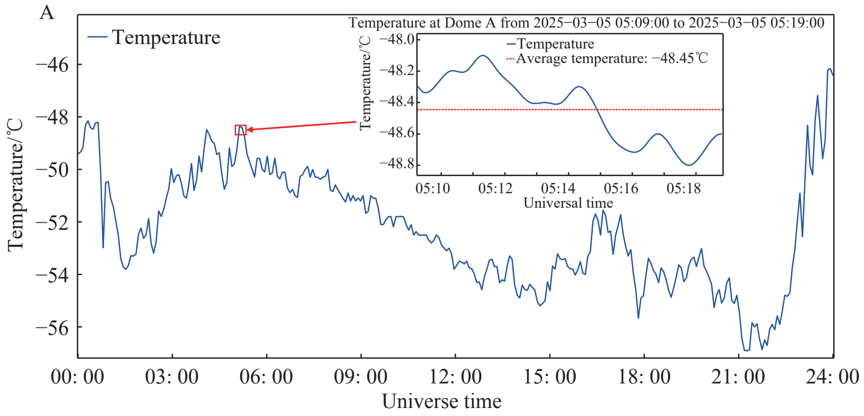

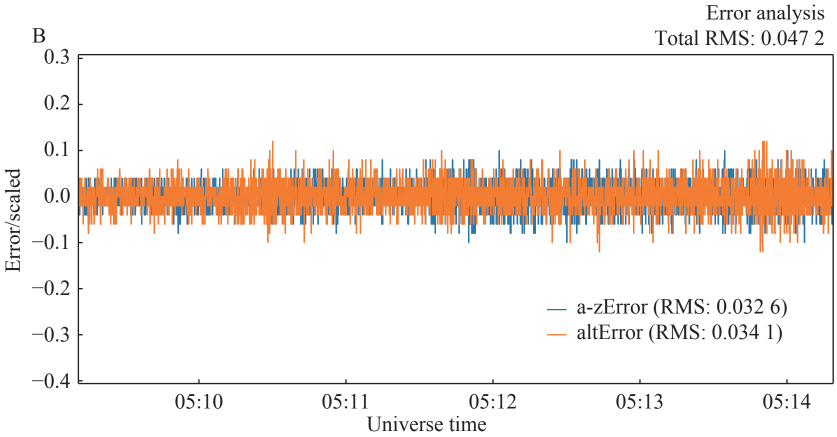

Fig. 14. Ambient temperature and motor encoder accuracy at Dome A, Antarctica, March 5, 2025. (A) Diurnal temperature record at Kunlun Station. (B) Encoder error of the motor during a 5-min period during the daytime temperature maximum.

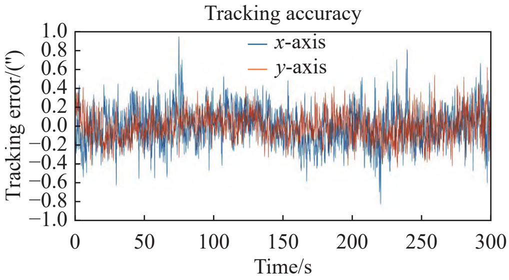

Fig. 15. Tracking error curve after calibration at Dome A.

vations in Antarctica but also provides valuable insight for the development of motor systems for other extreme environments.

ACKNOWLEDGEMENTS

This work was supported by the Space Debris Research Project, China (KJSP2020010102) and the National Key R&D Program of China (2022YFC2807300).

AI DISCLOSURE STATEMENT

Deepseek was employed for language and grammar checks within the article. The authors carefully reviewed, edited, and revised the Deepseek generated texts to their own preferences, assuming ultimate responsibility for the content of the publication.

AUTHOR CONTRIBUTIONS

Zhengyang Li led the project. Qingshan Li designed the structure of the motor, and Yao Zhang optimized the motor structure, proposed the motor simulation scheme, conducted the finite element analysis and simulation of the motor, and carried out various tests of the telescope motor with the help of Zhenshuai Yan. Xiaoyan Li led the writing of the manuscript and worked with Yao Zhang to complete the manuscript. Zhengyang Li installed the telescope at Kunlun Station in Antarctica. Yao Zhang and Jia'nan Cong remotely controlled the telescope and processed the operating data of the telescope. All authors read and approved the final manuscript.

DECLARATION OF INTERESTS

Zhengyang Li is an executive editor-in-chief for Astronomical Techniques and Instruments and he was not involved in the editorial review or the decision to publish this article. The authors declare no competing interests.

REFERENCES

[1] Lawrence, J. S., Ashley, M. C., Tokovinin, A., et al. 2004. Exceptional astronomical seeing conditions above Dome C in Antarctica. *Nature*, **431**: 278−281.

[2] Ma, B., Shang, Z. H., Hu, Y., et al. 2020. Night-time measurements of astronomical seeing at Dome A in Antarctica. *Nature*, **583**: 771−774.

[3] Wu, Z. X., Chen, C., Jiang, P., et al. 2024. Progress of the Antarctic large field of view telescope. *Chinese Journal of Polar Research*, **36**(1): 84−98. (in Chinese)

[4] Hu, Y., Shang, Z., Ashley, M. C., et al. 2014. Meteorological data for the astronomical site at Dome A, Antarctica. *Publications of the Astronomical Society of the Pacific*, **126**(943): 868.

[5] Gao, Y. T., Qu, R. H., Li, D. W., et al. 2016. Design of a dual-stator LTS vernier machine for directdrive wind power generation. *IEEE Transactions on Applied Superconductivity*, **26**(4): 5204505.

[6] Yin, X., Fang, Y. T., Huang, X. Y., et al. 2016. Analytical modeling of a novel Vernier pseudo-direct-drive permanent-magnet machine. In Proceedings of 2016 IEEE Conference on Electromagnetic Field Computation (CEFC).

[7] Bumby, J., Martin, R. 2005. Axial-flux permanentmagnet air-cored generator for small-scale wind turbines. *IEE Proceedings-Electric Power Applications*, **152**(5): 1065−1075.

[8] Dong, C. Y., Yang, Z. F., Ge, B. J., et al. 2024. Research on mechanism of electromagnetic performance changesin silicon steel core of low temperature high speed

permanentmagnet motors. *Electric Machines and Control*, **28**(9): 95−105. (in Chinese)

[9] Zhang, Y. P., Wang, Y. M., Gao, S. N. 2021. 3-D magnetic equivalent circuit model for a coreless axial flux permanent-magnet synchronous generator. *IET Electric Power Applications*, **15**(10): 1261−1273.

[10] Du, F. J., Zhang, J., Wen, H. K. 2014. Analysis, testing, and control of telescope's high-precision drive system in low-temperature environment. In Proceedings of SPIE, 9151: 1088–1094.

[11] Cyriac, F., Lugt, P., Bosman, R. 2016. Yield stress and low-temperature start-up torque of lubricating greases. *Tribology Letters*, **63**: 6.

[12] Du, F. J., Li, P. H. 2018. Effect of material expansion coeffcient and lubrication on telescope load torque under low temperature . *Optics and Precision Engineering*, **26**(3): 616−623. (in Chinese)

[13] Li, Z. Y., Cong, J. N., Wu, Z. X., et al. 2024. System design for a wide field-of-view near-infrared telescope for Dome A in Antarctica. *Publications of the Astronomical Society of the Pacific*, **136**(11): 115002.